JOURNAL OF MATERIALS RESEARCH AND TECHNOLOGY 2023;25:5003–5020

Available online at www.sciencedirect.com

jmr&t Journal of Materials Research and Technology

journal homepage: www.elsevier.com/locate/jmrt

Surface removal of ductile metal using cyclic low-frequency impact of a discrete particle-less waterjet

Zu'an Wang [a], *Yinze Lei* [a], *Jing Xie* [a,*], *Pengfei Wang* [b], *Gan Feng* [c], *Yong Kang* [b], *Pengwan Chen* [a,**], *D. Rittel* [d]

[a] *State Key Laboratory of Explosion Science and Technology, Beijing Institute of Technology, 100081 Beijing, PR China*
[b] *Hubei Key Laboratory of Waterjet Theory and New Technology, Wuhan University, 430072 Wuhan, PR China*
[c] *State Key Laboratory of Hydraulics and Mountain River Engineering, Sichuan University, 610065 Chengdu, PR China*
[d] *Faculty of Mechanical Engineering, Technion - Israel Institute of Technology, 32000 Haifa, Israel*

ARTICLE INFO

Article history:
Received 9 May 2023
Accepted 2 July 2023
Available online 5 July 2023

Keywords:
Discrete waterjet
Cyclic liquid impact
Material removal
Surface morphology
Erosion mechanism

ABSTRACT

The discrete waterjet (DWJ) offers advantages in material removal because of the cyclic impact loading, but the specific removal characteristics and corresponding mechanisms have not been yet fully understood. Therefore, the flow field and material removal characteristics of the DWJ were studied through numerical and experimental methods, including the velocity and impact pressure distribution, surface morphology, quantitative statistics of erosion crater, and fractography under different jet pressures and exposure times. The results indicate that mechanical interruption has a positive impact on increasing the maximum velocity (53.0% at 30 MPa) of the waterjet head and altering the impact pressure distribution, resulting in an asymmetric erosion crater with a tapering groove along the edge. Meanwhile, the DWJ has superior working efficiency (higher erosion area, depth and volume) and energy utilization (lower specific energy) than the continuous waterjet (CWJ), while avoiding the unfavorable high crater lips. A large amount of material removal does not necessarily occur in the initial stage of waterjet impact, and it is related to material properties, waterjet parameters and specific evaluation indexes. The increase of waterjet pressure accelerates the material removal process and improves the energy consumption efficiency. The materials removing process is divided into four stages: surface deformation due to the cyclic impact pressures, surface break-ups localized near the surface unevenness, independent fragment forming mainly by water wedge pressure, and larger removal of materials due to these cyclic processes.

1. Introduction

The abrasive waterjet has long been commercialized and applied in the fields of rock mining [1,2], surface treatment [3,4] and material removal [5,6], because it has the advantages of no thermal distortion [7], high flexibility [8], and high machining versatility [9]. However, for the typical post-mixing (introducing the abrasives after the acceleration stage of water flow, as opposed to the pre-mixing that the abrasives mixed

* Corresponding author.
** Corresponding author.
E-mail addresses: jxie@bit.edu.cn (J. Xie), pwchen@bit.edu.cn (P. Chen).
https://doi.org/10.1016/j.jmrt.2023.07.008

Nomenclature

CWJ	Continuous waterjet
DWJ	Discrete waterjet
P_h	Water hammer pressure
ρ_1, ρ_2	Densities of liquid and target
c_1, c_2	Shockwave velocities in liquid and target
v	Waterjet velocity
t	Exposure time
P_s	Stagnation pressure
v_m	Linear velocity of disc
ω	Rotation speed
S	Standoff distance
S_{dt}	Disc-to-target distance
S_{dn}	Disc-to-nozzle distance
d	Nozzle diameter
D_i	Inlet diameter
θ	Convergent angle
D_x	Diffusion diameter
φ	Divergence angle of waterjet
D_s	Interruption diameter
f_h, f_t	Dissipation coefficient of velocity for jet head and tail
N	Slot number
W_t	Slot width
W_k	Spoke width
u_{eff}	Effective viscosity
$\overrightarrow{F}$	Term of interfacial force source
k	Turbulent energy
σ_k, σ_ε	Prandtl number
u_t	Turbulent viscosity
f	Frequency
p	Supply pressure
l	Slug length
E_t	Total energy
V_h	Volume of jet head
V_t	Volume of jet tail
V_m	Waterjet volume of main part
V_s	Total volume of single slug
l_m	Length of main part
p_{max}	Maximum static pressure during waterjet impact
x	Horizontal coordinate on impact surface
$p(x,0)$	The pressure at distance x
A_c, $\dot{A_c}$	Crater area and its growth rate
D_c, $\dot{D_c}$	Crater depth and its growth rate
V_c, V_{cp}	Crater volume and its growth rate per slug
E_s	Specific energy
E_{sp}	Specific energy per slug
H_p	Maximum height of the lips
P_c	Crater perimeter
z	Depth coordinates on target material
C_i	Circularity
VOF	Volume of fluid
UDF	User defined function
$\overrightarrow{v}$	Velocity vector
α_q	Volume fraction of phase q
ε	Turbulent dissipation rate
P_k, G_b	Turbulent energy generated by velocity gradient and buoyancy
Y_M	Fluctuation term

with water before the acceleration) abrasive waterjet, the abrasive particles are not always uniformly mixed in the high-speed waterjet [10]. Some abrasives are not fully wetted and accelerated, which reduces the working efficiency of the waterjet. In some cases, a small number of abrasive particles might be embedded in the material surface, causing stress concentrations and subsequent reduction of fatigue life [11,12]. To avoid these problems, an effective way consists of using *high-efficiency pure waterjet* instead.

The process of waterjet impacting on the target includes two stages: the water hammer pressure stage (Stage I) and the stagnation pressure stage (Stage II) [13], as shown in Fig. 1. During Stage I, a pressure pulse occurs in the center area of the target due to the transient fluid compression, with the peak pressure value being called water hammer pressure [14,15], and it can be expressed as:

$$P_h = \frac{\rho_1 c_1 \rho_2 c_2 v}{\rho_1 c_1 + \rho_2 c_2} \tag{1}$$

where P_h is the water hammer pressure, ρ_1, ρ_2 and c_1, c_2 are the densities and shockwave velocities in the fluid and target material, respectively, and v is the incoming jet velocity.

For a completely rigid target, the pressure can be expressed:

$$P_h = \rho_1 c_1 v \tag{2}$$

As the transient compression energy releases in the central area, the impact pressure decreases to a relatively steady stagnation pressure P_s in stage II:

$$P_s = \frac{1}{2}\rho_1 v^2 \tag{3}$$

The relatively low steady stagnation pressure is already insufficient to neither strip nor cut the target. The motivation of maintaining high impact pressure drives the researchers to increase the waterjet velocity by elevating the pressure of pump as much as possible. Nevertheless, there is an upper limit of pump pressure due to the sealing performance and the equipment cost. An alternative approach to keeping high working pressure is to generate a discontinuous pressure pulse. The *discrete waterjet* (DWJ), therefore, appears to provide a potential method of processing materials under relatively low pump pressure by exerting pulsed loads on the target surface. The DWJ owns excellent dynamic load characteristics [16–18], including the cyclic water hammer pressure [19], stress wave effects [20], and dynamic lateral jetting [21], which is suitable for cleaning, coating stripping and other applications in surface material removal.

DWJ can be generated by different methods. One popular method is to design a special nozzle structure to generate a self-excited oscillating waterjet [22]. This delicate-designed

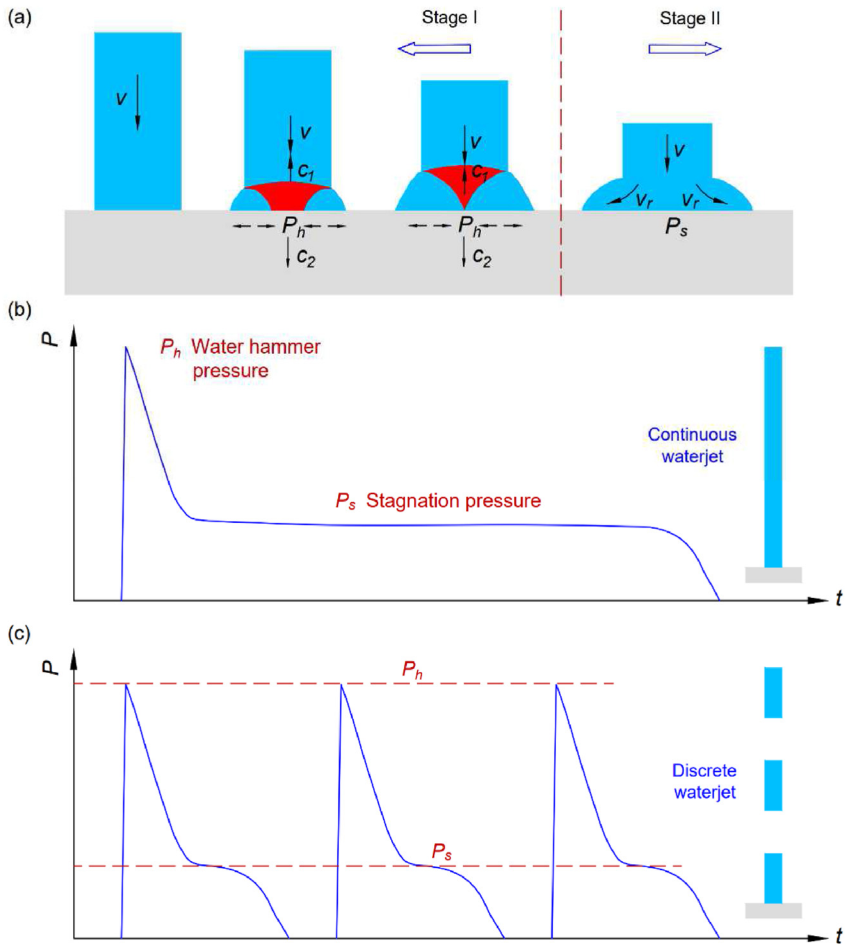

Fig. 1 – Schematic diagram of pressure changes during liquid impingement. (a) Liquid impact process; (b) pressure change of CWJ; (c) pressure change of DWJ.

nozzle can be easily combined with other equipment such as drilling tools and shield tunneling machines to enhance working efficiency. Another well-accepted way is using a stimulation source to generate pulsation in the flow field. For example, the ultrasonic wave as a stimulation resource can generate a jet pulsation with a frequency greater than 20 kHz. Foldyna et al. [23] studied the erosion performance of the ultrasonically modulated waterjet, and reported a marked increase of mass loss. Hloch et al. [24] and Srivastava et al. [25] further investigated the ductile erosion of different metals, and considered that the ultrasonically modulated waterjet can be used for surface modification, determination of erosion resistance, and disintegration of biomedical materials. The ultrasonic wave endows the pulsed waterjet with excellent impact characteristics, but the strong correlation between oscillation intensity and supply pressure creates challenges to controlling the load strength.

Scholars in the Cavendish Laboratory creatively placed a slotted rotating disc downstream of the nozzle to interrupt the continuous flow to obtain the DWJ [26]. Despite its original purpose being the quantitative analysis of material erosion, the idea behind the design eventually evolved into a means of cutting materials using DWJ [27]. In this way, the jet parameters are independent of each other, so it is easier to accurately control the load intensity. Vijay et al. [28] showed that this method has the potential of fragmenting hard rocks, and defined it as a processing tool with promising applications. Jackson [29] conducted many experiments to investigate the theoretical machining threshold curve of brittle materials, and he proposed the use of discrete liquid impact to achieve micro and nanomanufacturing. Dehkhoda et al. [30,31] conducted systematic experiments to investigate the performance of the DWJ and found the synergistic effects of slug length and waterjet frequency on damage development. Other scholars further studied the effects of working parameters, such as nozzle diameter, standoff distance, and interruption parameters on the erosion characteristics [32,33]. Under mechanical interruption, the characteristics of the discrete water volume can be controlled or modified, such as the jet length, the frequency, the shape of the flow field, and the number of jet impacts. The mechanical interruption makes it more flexible to adjust the jet structure, and these adjustments are completely controllable. This provides an idea to achieve a precise control of material removal by adjusting the characteristic parameters of the jet [34]. Yamagata et al. [35] investigated the erosion behavior of DWJ on aluminum, providing a reference for erosion resistance testing of wind turbine blades.

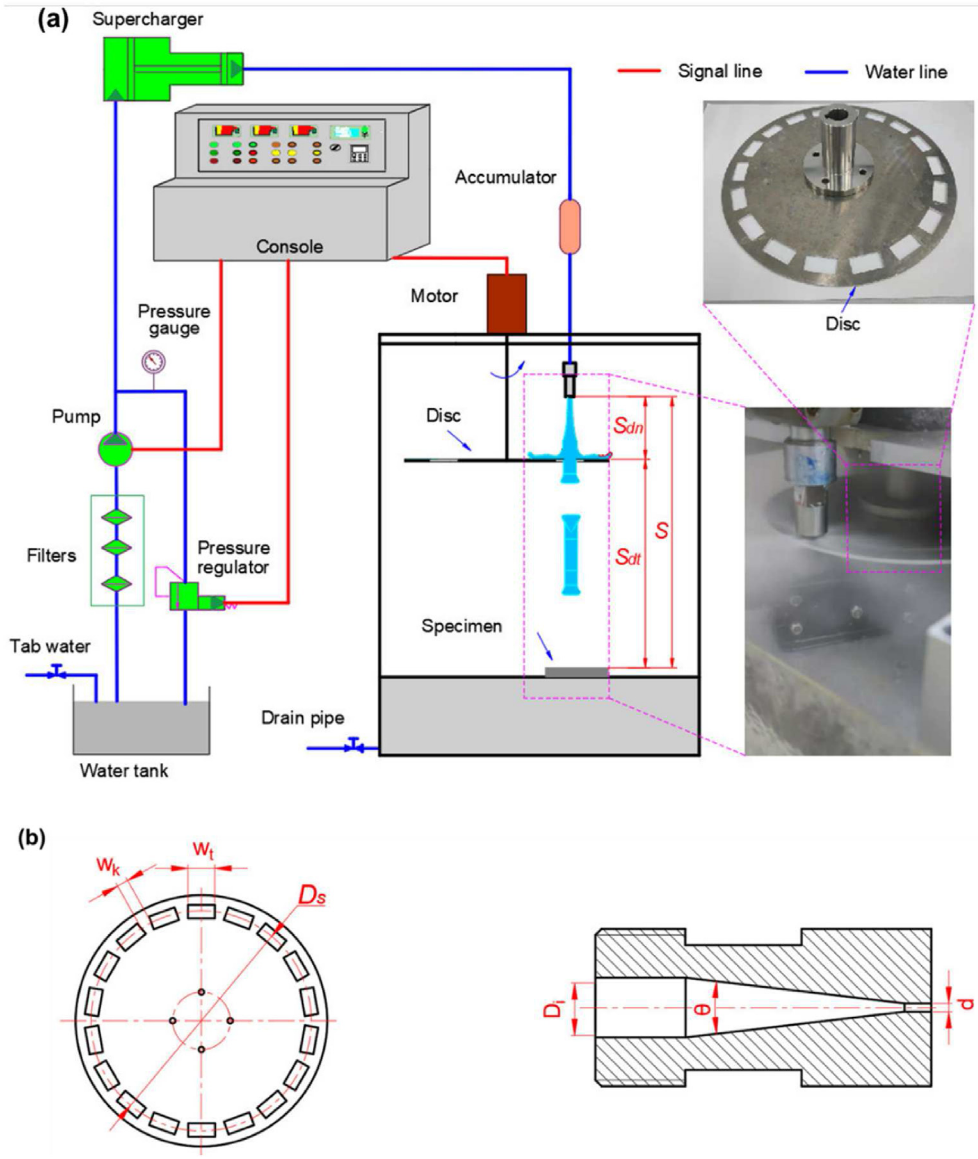

Fig. 2 – Schematic diagram of the experimental system. (a) Jet generation system; (b) structure diagram of disc and nozzle.

The above mentioned studies broadly confirm the potential for wide-ranging applications of DWJ, but the material removal mechanism is still incompletely understood, which requires a more comprehensive understanding of the temporal-spatial evolution characteristics of DWJ. Therefore, the flow field and material removal characteristics of the DWJ were studied comprehensively. Section 2 introduces the waterjet system, experiment scheme, and the details of numerical simulation. In section 3, the velocity and impact pressure distribution, surface morphology, quantitative statistics of material removal, and fractography were investigated. Finally, section 4 discusses the material removal

Table 1 – Equipment parameters.

Rotation speed ω (r/min)	Standoff distance S (mm)	Disc-to-target distance S_{dt} (mm)	Slots number	Outlet diameter D_o (mm)	Inlet diameter D_i (mm)	Convergent angle θ (°)	Interruption diameter D_s (mm)
400	40	24	18	0.5	6	13	220

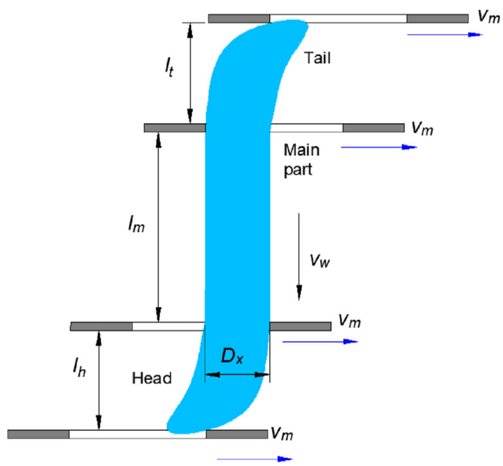

Fig. 3 – Schematic diagram of a single water slug [33].

mechanism from the loading patterns and evolutionary target characteristics.

2. Materials and methods

2.1. *Erosion experiment*

The experiment was carried out on a multifunctional test bench, as shown in Fig. 2. Overall, the bench consists of a high-pressure system for generating waterjet, a control system for monitoring and controlling the system parameters and an interruption system for discretizing the CWJ. A hydraulic supercharger was used to pressurize the water to a convergent nozzle through pipelines. The accumulator in the high-pressure system can reduce the pressure pulsation caused by high pressure pumps. Moreover, to prevent pressure fluctuation caused by pipeline bending, the pipeline near the nozzle inlet was arranged vertically and collinear with the nozzle axial. In the control system, the signals of supply pressure, flow rate, and rotating speed are transmitted to a console through signal lines. A rotating disc was placed in front of the nozzle, and its axial direction was parallel to the waterjet. Jet frequency and slug length were regulated by the modulated parameters (slot number, width, and rotation speed) at 120 Hz and 438 mm, respectively. The standoff distance (S) was kept at 40 mm, and the disc-to-target distance (S_{dt}) was 24 mm, as listed in Table 1.

After mechanical interruption, the overall structure of a single water slug is composed of three parts: waterjet head, main part and waterjet tail, as shown in Fig. 3. From a kinematic perspective, the formation time of the waterjet head is equivalent to the time required for the disc to move the distance of the waterjet diameter. Defining the waterjet diameter as D_x and linear velocity of the disc at the interruption position as v_m, the time of waterjet head formation (t_p) can be expressed using the following equation:

$$t_p = \frac{D_x}{v_m} \tag{4}$$

With the inclusion of waterjet diffusion, the waterjet diameter at the modulation position can be represented as:

$$D_x = 2S_{dn} \tan\frac{\varphi}{2} \tag{5}$$

where φ is the diffusion angle (usually 27–30°), and Sdn is defined as the disc-to-nozzle distance.

The length of the main part of the water slug can be expressed as:

$$l_m = v\frac{W_t - 2D_x}{v_m} \tag{6}$$

where the W_t is the slot width of the disc.

Table 2 – Specific experimental parameters.

Sample no.	Jet type	Slot width W_t (mm)	Spoke width W_k (mm)	Supply pressure p (MPa)	Exposure time t (s)	Frequency f (Hz)	Slug length l (mm)
S1	DWJ	11.7	26.7	15	60	120	438
S2	DWJ	11.7	26.7	15	120	120	438
S3	DWJ	11.7	26.7	15	300	120	438
S4	DWJ	11.7	26.7	15	600	120	438
S5	DWJ	10.1	28.2	20	60	120	438
S6	DWJ	10.1	28.2	20	120	120	438
S7	DWJ	10.1	28.2	20	300	120	438
S8	DWJ	10.1	28.2	20	600	120	438
S9	DWJ	9.0	29.3	25	60	120	438
S10	DWJ	9.0	29.3	25	120	120	438
S11	DWJ	9.0	29.3	25	300	120	438
S12	DWJ	9.0	29.3	25	600	120	438
S13	DWJ	8.2	30.1	30	60	120	438
S14	DWJ	8.2	30.1	30	120	120	438
S15	DWJ	8.2	30.1	30	300	120	438
S16	DWJ	8.2	30.1	30	600	120	438
S17	CWJ	–	–	15	600	–	–
S18	CWJ	–	–	20	600	–	–
S19	CWJ	–	–	25	600	–	–
S20	CWJ	–	–	30	600	–	–

Table 3 – Mechanical properties and composition (wt. %) of material.

Tensile strength (MPa)				Vickers hardness		Density (g/cm^3)	
85				34–40		2.70	
Fe	Si	Cu	Mn	Mg	Zn	Ti	Al
≤0.15%	≤0.15%	≤0.03%	≤0.02%	≤0.02%	≤0.03%	≤0.03%	Remaining

When factoring in the impact of the interaction between the jet flow and rotating disc on the waterjet velocity, the length of the waterjet head and tail can be expressed as:

$$l_h = v t_p f_h \tag{7}$$

$$l_t = v t_p f_t \tag{8}$$

where f_h and f_t denote the velocity attenuation coefficients (ranging from 0.95 to 1) during the generation of the waterjet head and tail, respectively.

Thus, the length of a single water slug can be obtained:

$$l = v\frac{W_t + 2(f_h + f_t - 2)S_{dn}\tan\frac{\varphi}{2}}{v_m} \tag{9}$$

Within the idealized mathematical model, the volume of the waterjet head and tail structure is assumed to be equal and can be represented as:

$$V_h = v_w \int_0^{D_x/v_m} \left[\frac{D_x{}^2}{4}\arcsin\left(\frac{v_m t - 0.5D_x}{r}\right) + (v_m t - 0.5D_x)\sqrt{v_m t(D_x - v_m t)} + \frac{\pi D_x{}^2}{8}\right]dt \tag{10}$$

The volume of main part of a single slug can be represented by the following formula:

$$V_m = l_m\frac{\pi d^2}{4} \tag{11}$$

The volume of single water slug can be obtained:

$$V_s = 2V_h + V_m \tag{12}$$

The total energy (E) of the DWJ can be expressed:

$$E_t = \frac{tf\rho v^2 V}{2} \tag{13}$$

Based on the above equipment parameters, the specific experimental parameters of DWJ were listed in Table 2. To comprehensively explore the material removal process of the ductile surface by low-frequency waterjet impact, 1080 Al (99.8% purity aluminum) was selected as the evaluation material. The mechanical properties and material composition are listed in Table 3. Aluminum samples with a size of 40 × 40 × 4 mm were fixed on the precision lifting base. The target was exposed to the DWJ under different exposure times and jet pressures. A baffle was used to isolate the impact of the waterjet on the sample before reaching the set pressure. The experiment was repeated 2–4 times under the same experimental conditions. The standard deviations of erosion parameters were calculated.

2.2. *Characterization methods*

The sample morphology was observed using optical profilometry (μ-scan, Nano Focus AG, Oberhausen), using a focal size of 20 μm × 20 μm. The profilometer was used to obtain the longest section profile, as well as to obtain measurements for the coverage area (A_c), crater depth (D_c), height of protuberant lips (H_p), and crater volume (V_c). To evaluate the energy efficiency, the specific energy E_s was calculated to evaluate the energy consumption of the DWJ [36].

$$E_s = \frac{E_t}{V_c} \tag{14}$$

At the same time, the entrance circularity C_i of the erosion crater was calculated according to the data obtained by the profiler. When equal to 1, the crater entrance is a perfectly symmetrical circle [37].

$$C_i = \frac{4\pi A_c}{P_c^2} \tag{15}$$

where P_c is the perimeter.

Finally, the resulting surface was examined using scanning electron microscopy (TESCAN, Mira 3, Kohoutovice), to identify the mechanisms of ductile material removal due to the cyclic impact of low-frequency DWJ.

2.3. *Numerical simulation*

As the impact performance of the waterjet is highly dependent on the magnitude and duration of impact pressure, which is closely linked to the flow field structure of the waterjet, the formation process of mechanically interrupted waterjets was simulated through a two-dimensional computational model with FLUENT software to better understand the interaction between the jet and target [38]. Because the numerical simulation was only used to analyze the flow field structure during the impact process, the transient nonlinear deformation of the water was not considered. The water and air materials were set as the ideal incompressible fluids selected from the FLUENT DATABASE (water-liquid (h2o<l>)

Table 4 – Liquid properties.

	Density (kg/m^3)	Viscosity (kg/(m.s))	Molecular weight (kg/kmol)	Reference temperature (K)
Water	998.2	0.001003	18.0152	298
Air	1.225	1.7894e-5	28.966	298

and air, as listed in Table 4). The simulation was based on the computational fluid dynamics method, with the VOF (volume of fluid) multiphase flow model and realizable k-ε turbulence model being used to describe the fluid flow within the waterjet. As the fluid is assumed to be incompressible, the continuity and momentum equations are the only ones required to describe its flow [38]:

$$\frac{\partial \rho}{\partial t}+\nabla\cdot(\rho\vec{v})=0 \tag{16}$$

$$\rho\frac{\partial\vec{v}}{\partial t}+\rho\vec{v}\cdot\nabla\vec{v}=-\nabla p+\rho g+\nabla\cdot u_{eff}(\nabla\vec{v}+\nabla\vec{v}^{T})+\vec{F} \tag{17}$$

where $\vec{v}$ represents the velocity vector, u_{eff} is the effective viscosity, and $\vec{F}$ denotes the term of interfacial force source.

The VOF model operates by solving a series of momentum equations while concurrently monitoring the volume fraction of each fluid within the computational domain. The determination of the interphase interface is achieved through the resolution of the volume fraction continuum equation, which accounts for the respective liquid-gas phases.

$$\frac{\partial \alpha_q}{\partial t}+\nabla\cdot(\alpha_q v)=0 \tag{18}$$

$$\sum_{q=1}^{2}\alpha_q=1 \tag{19}$$

where α_q denotes the volume fraction of phase q.

A realizable k-ε turbulence model includes k and ε transport equations:

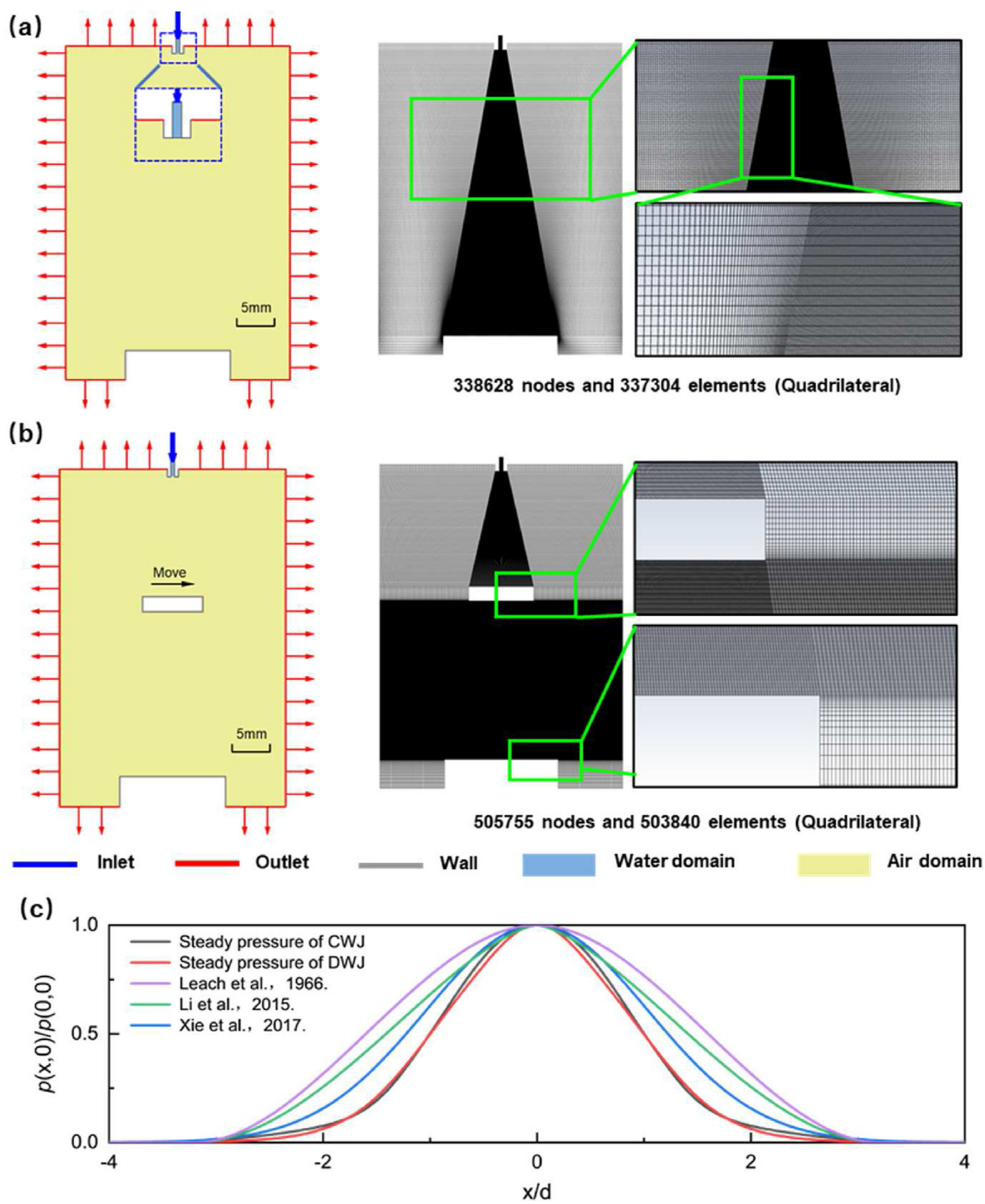

Fig. 4 – Computational model and verification. (a) Model structure and mesh of CWJ; (b) model structure and mesh of DWJ; (c) comparison of normalized pressure distribution.

Table 5 – Mesh smoothing and reconstruction parameters.

Diffusion smoothing			
Function	Diffusion parameter	Maximum iterations	Relative tolerance
Boundary distance	1.5	40	0.0001

Mesh reconstruction					
Method	Size function	Minimum length (mm)	Maximum length (mm)	Maximum skewness	Interval
Local element and surface	Resolution: 3 Variable: 2.675 Rate: 0.3	5e-3	0.138	0.7	5

$$\frac{\partial(\rho k)}{\partial t}+\frac{\partial\left(\rho k\overrightarrow{v}_j\right)}{\partial x_j}=\frac{\partial}{\partial x_j}\left[\left(u+\frac{u_t}{\sigma_k}\right)\frac{\partial k}{\partial x_j}\right]+P_k+G_b-\rho\varepsilon-Y_M \tag{20}$$

$$\frac{\partial(\rho\varepsilon)}{\partial t}+\frac{\partial\left(\rho\varepsilon\overrightarrow{v}_j\right)}{\partial x_j}=\frac{\partial}{\partial x_j}\left[\times\left(u+\frac{u_t}{\sigma_\varepsilon}\right)\frac{\partial\varepsilon}{\partial x_j}\right]+\rho C_1 S\varepsilon-\rho C_2\frac{\varepsilon^2}{k+v\varepsilon}+C_{\varepsilon1}\frac{\varepsilon}{k}C_{\varepsilon3}C_b+S_\varepsilon \tag{21}$$

where k and ε denote the turbulent energy and dissipation rate, respectively; σ_k *and* σ_ε are the corresponding Prandtl number; P_k and G_b are the turbulent energies generated by the velocity gradient and buoyancy, respectively; Y_M is fluctuation caused by excessive diffusion in compressible turbulence; u_t and v are the turbulent viscosity and kinematic viscosity, respectively; $C_{\varepsilon1}=1.44$, $C_2=1.9$, $C_{\varepsilon3}=1$.

$$u_t=C_u\rho\frac{k^2}{\varepsilon} \tag{22}$$

where the C_u is a constant equal to 0.09.

Numerical simulation was performed to compare the flow field structure of an ordinary CWJ and an interrupted water jet impacting the target. The model structure and the mesh information are shown in Fig. 4(a) and (b). The quadrilateral structured grids were used in both calculation models. To accurately capture the evolution of the waterjet structure and the distribution of impact pressure, we refined the grids in the area where the waterjet was passing. The grids near the target wall had the smallest characteristic size of 0.02 mm. To maintain computational stability, we employed a smooth transitional approach between different regional grid sizes, with a maximum growth ratio of 1.2. The dynamic grid model was used to achieve the boundary movement, and the movement parameters were defined on the grid surface using User Defined Functions (UDFs). The mesh reconstruction and diffusion smoothing algorithm were used for the wall movement, and details were shown in Table 5.

The inlet boundary was set as a pressure condition (30 MPa), with the turbulent state determined by the turbulent intensity and hydraulic diameter. The pressure outlet boundary condition is applied at the side of the air domain, as shown in Fig. 4. The target surface located 40 mm away from the waterjet inlet is modeled as a smooth no-slip wall. Meanwhile, to improve computation accuracy, the second-order upwind scheme was used for the iterative solution. To capture fine details in the flow field and save computational resources, adaptive time stepping with mesh deformation control was used with a range of 10^{-7}-10^{-6}s.

The validity of the models was confirmed by comparing the distribution of normalized impact pressure in a steady state, as presented in Fig. 4(c). The parameter $p(0,0)$ represents the pressure at the impact center of the jet flow, and it is the maximum value during the stabilization stage along the target surface. The stable impact pressure of DWJ was observed to be similar to that of CWJ, with both following a normal distribution. By comparing the normalized pressure distribution attained from the aforementioned model with that of related models introduced by other scholars, it was observed that these pressure distributions exhibited a high degree of consistency. Both of their distributions exhibited a Gaussian

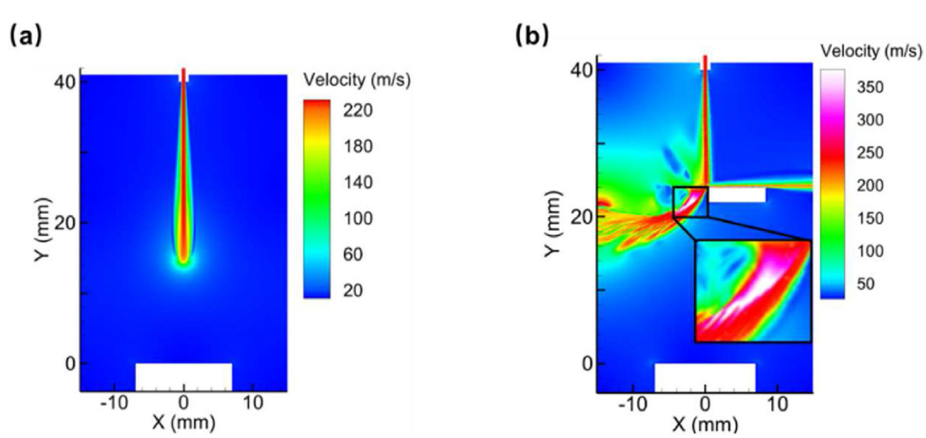

Fig. 5 – Velocity distributions of CWJ (a) and DWJ (b).

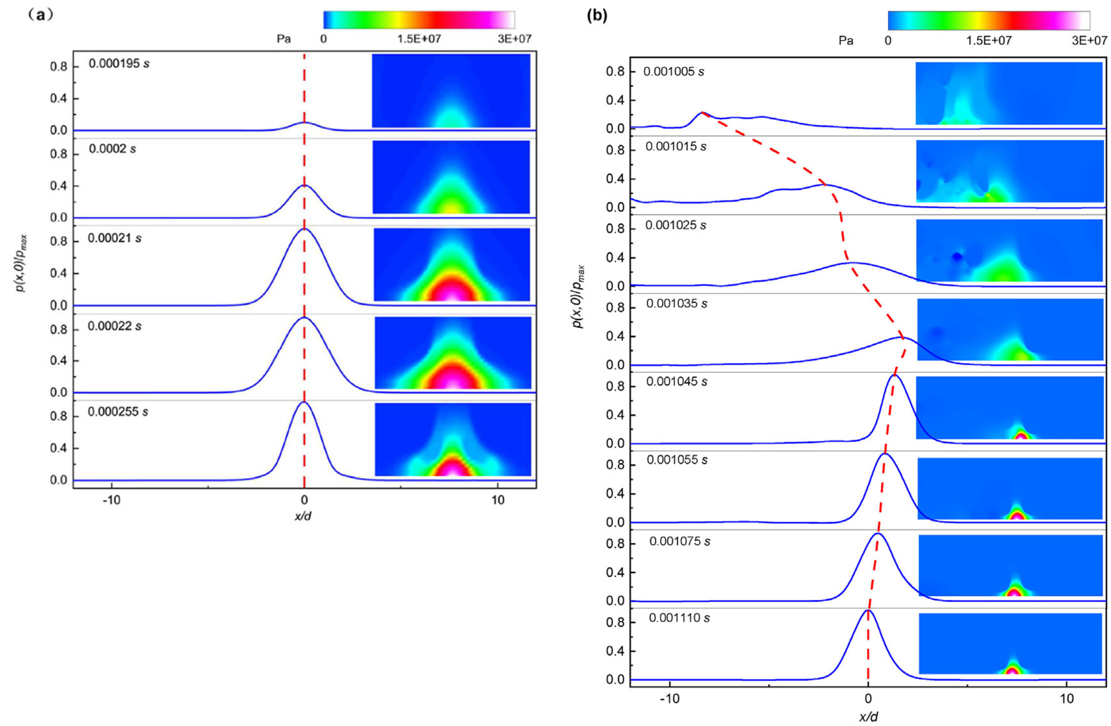

Fig. 6 – Comparison of normalized pressure distribution of CWJ (a) and DWJ (b).

shape, possessing a comparable half-height width of approximately 3. These results confirm the reliability of numerical calculation models of CWJ and DWJ in this paper.

3. Results

3.1. Flow field simulations

The velocity distributions of CWJ and DWJ at 30 MPa are shown in Fig. 5. The first difference between the two jets is the symmetry of the waterjet head and velocity distribution. The difference in the velocity distribution means that the impact patterns of the two jets are different in the initial period. Secondly, through the legends, it can be clearly found that the velocity of the jet head of DWJ is higher than that of the CWJ. In the generation process of DWJ, the blocked part of the waterjet body will produce a lateral velocity and increase the overall speed of the unblocked part. The deflection of the waterjet head is highly consistent with the previous models, and the difference is that the waterjet head of DWJ gets separated due to the finite liquid tension and tends to form smaller droplets. It is foreseeable that this change will inevitably affect the material removal process, and further details will be discussed in conjunction with the results of target material removal.

Then, the normalized impact pressure of the two waterjets with the normalized lateral distance is shown in Fig. 6(a) and (b), respectively. For the CWJ, the impact pressure on the target wall is highly symmetric with Gaussian distribution. From the initial impact to the steady stage, the pressure in the impact area shows a gradual upward trend, and the area of local high pressure increases first and then decreases. For the DWJ, due to the special flow field structure, the position of the peak pressure moves on the target surface. It means that the mechanical interruption makes the DWJ have a horizontal feed speed when the nozzle is still, which is beneficial to weaken the water cushion effect and expand the material removal range. Meanwhile, combined with the flow field structure and normalized pressure amplitude, the impact pressure of the main part of water slug is much higher than that of deflected waterjet head for DWJ. It should be noted that the distribution of stable pressure on target surface eventually tends towards Gaussian distribution, consistent with the CWJ.

3.2. Surface morphology

The three-dimensional morphologies caused by the CWJ (S20) and DWJ (S6, S8, S14, and S16) are shown in Fig. 7. For S20, the crater entrance is nearly circular due to the approximately axisymmetric structure of the CWJ, and protuberant lips are observed on the sample surface. Although the complete isotropies of the target material and the generated waterjet cannot be guaranteed, the entrance circularity of the erosion crater generated by the CWJ still reaches 0.652, and it matches the reported results for the symmetrical erosion craters of CWJ [39]. For the crater formed by the DWJ, the surface morphology, a short tapering groove appeared as reported previously in the brittle targets. In addition, the protuberant lips also occurred on the edges of the tapering groove due to the oblique impact of the waterjet head. The circularity of the crater entrance decreases with the exposure time and waterjet pressure, and the circularity is only 0.486 on S8 ($p = 20$ MPa, $t = 600$s) and 0.422 on S16 ($p = 30$ MPa, $t = 600$s).

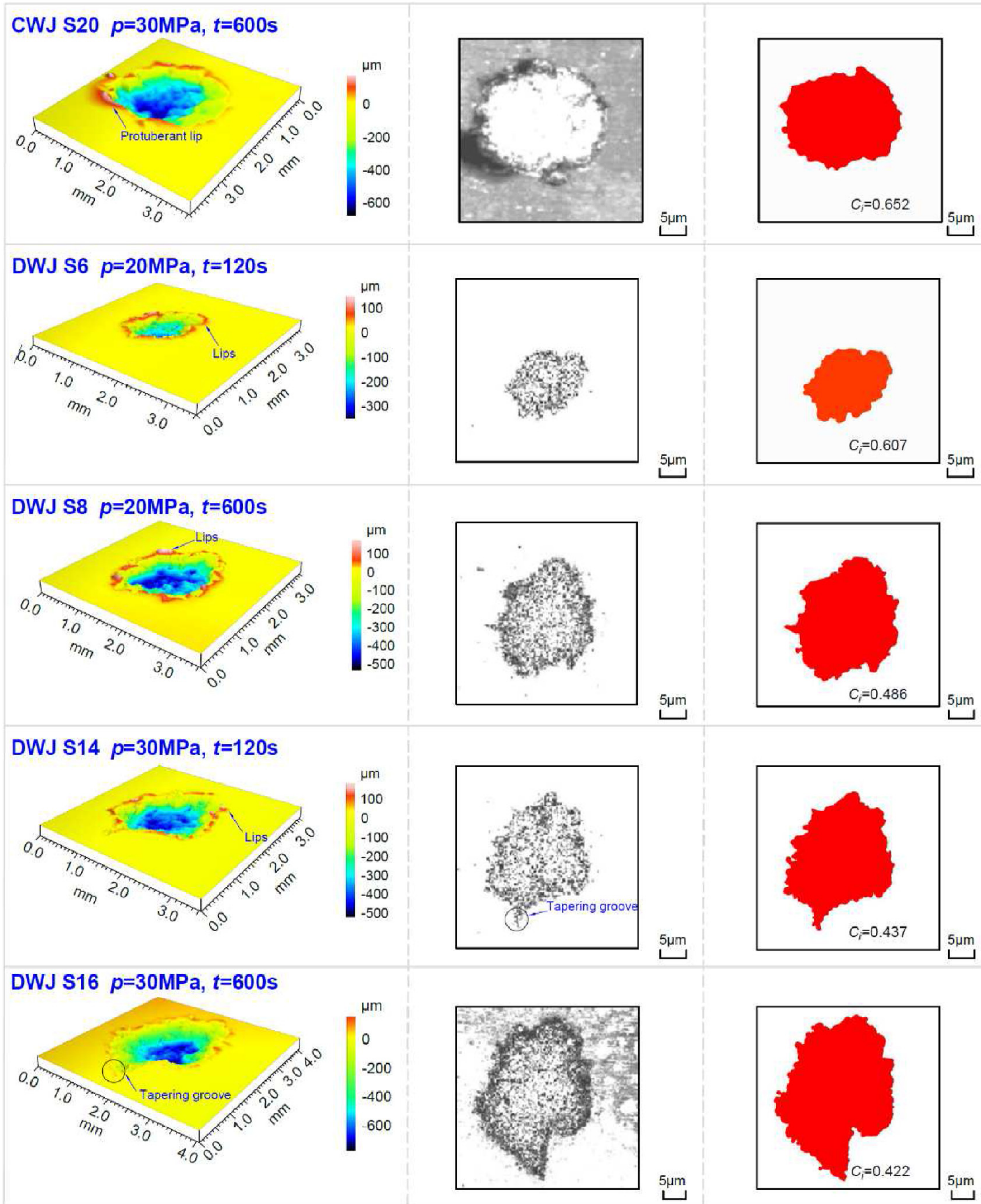

Fig. 7 – Surface morphology of CWJ and DWJ. As 3D profile shows, there are significant protuberant lips (also called shearing lips, red color parts in the images) that surrounds the crater, leading to the initiate material removal by shear damage.

Since pressure is asymmetric initially, material removal becomes increasingly significant as the exposure time and waterjet pressure increase.

Next, the section profiles of the erosion crater were extracted to study the inner wall evolution. As shown in Fig. 8, the section profiles are U-shaped with ragged peaks and valleys. Below 120s (S13, S14), the process of material removal primarily results in an increase in the crater depth, while the crater span (as shown in Fig. 8) does not vary significantly. As the exposure time increases above 120s (S14, S15, S16), the material removal mainly causes changes in the crater span. Below 600s, the increase in waterjet pressure leads to a synchronous increase in both the crater span and depth (S4, S8, S12 and S16). Additionally, compared to CWJ (S20), the main differences in the section profiles formed by DWJ (S16) are the asymmetries of the wall slopes and the appearance of the tapering groove.

In order to comprehensively demonstrate the material removal characteristics of the DWJ, the surface morphology isotropies of the erosion crater were measured at 60, 120, 300,

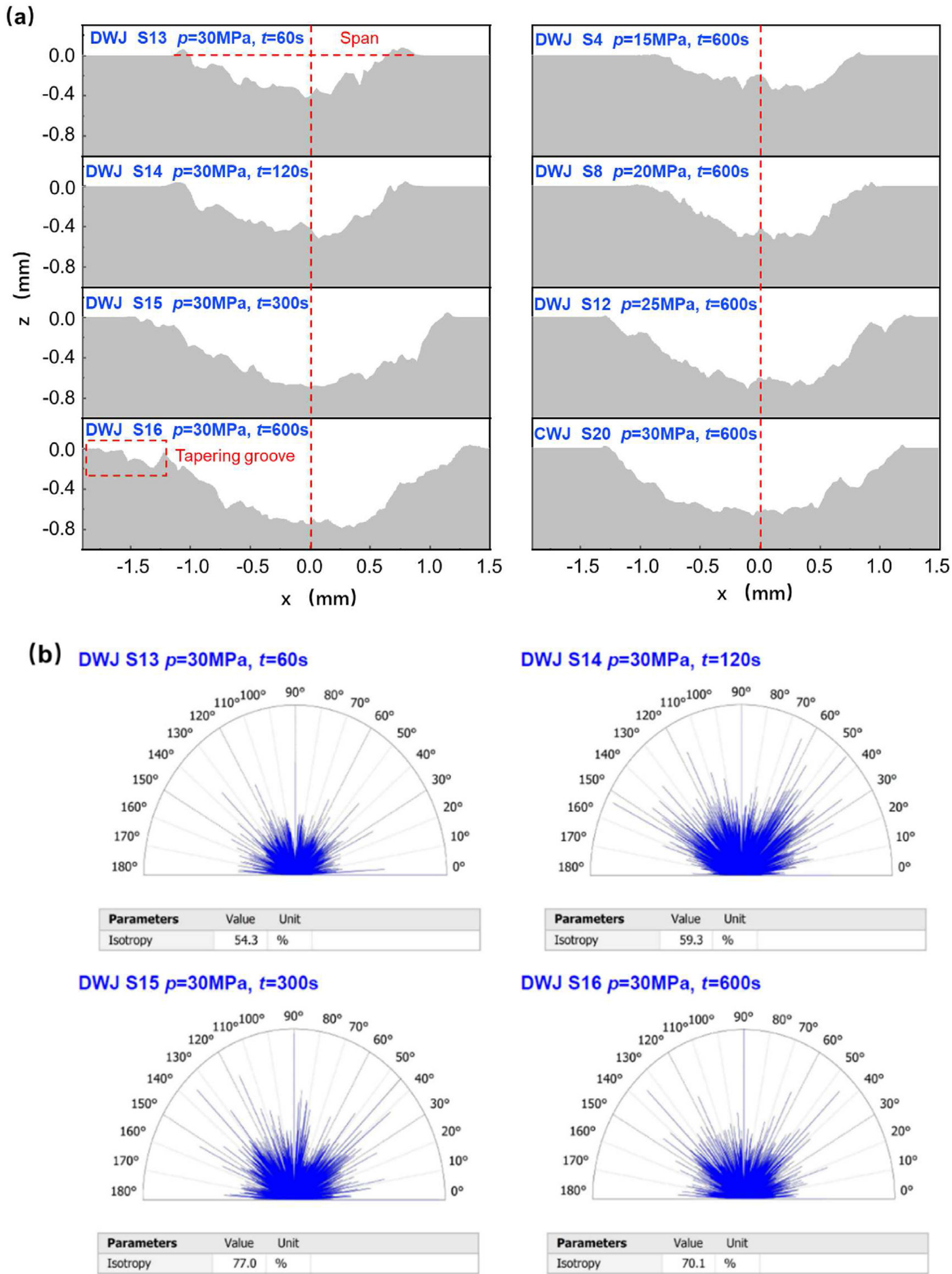

Fig. 8 – (a) 2D profiles of DWJ (S4, S8, S12, S13, S14, S15, S16) and CWJ (S20); (b) angular spectrum image and isotropies. Note that the spectrum is used to describe the direction of surface texture, if the value of Isotropy equals to 100% the surface is a complete isotropy surface, whilst the value of anisotropy surface is near zero.

and 600s under 30 MPa (S13, S14, S15 and S16), as shown in Fig. 8(b). A value of 100% for isotropy means that the erosion strength is uniform across all directions of the sample surface within a 360° range. In the figure, the isotropy of the target surface fluctuates significantly with the exposure time. At 300s, the isotropy reaches the peak value of 77.0%. After the development of the tapering groove, the isotropy decreases to 70.1%, which implies that the material removal by the DWJ is more prominent in the direction of waterjet deflection.

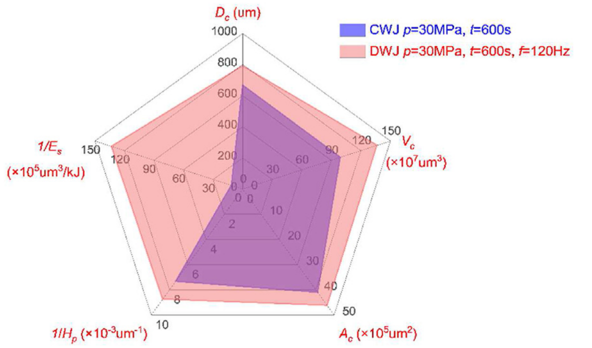

Fig. 9 – Comparison of CWJ and PWJ. For parameters of D_c, V_c and A_c, the higher the better; on the contrary, for parameters of H_p and E_s, the lower the better, so the inverse of H_p and E_s are used instead to demonstrate the advantages of DWJ in material removal.

3.3. *Quantitative statistics*

3.3.1. CWJ vs. DWJ

The DWJ not only has completely independent and controllable technological parameters (pressure, exposure time, frequency and slug length), but also shows superior performance to CWJ in material removal. Fig. 9 compares the material removal performances of CWJ and DWJ under 30 MPa (S20 and S16). Firstly, analysis of erosion crater sizes reveals that DWJ has a superior material removal performance in terms of coverage area, crater depth, and erosion volume. It means the impact performance can be improved by discretizing the continuous flow. In addition, a comparison of the height of protuberant lips between CWJ and DWJ demonstrates that the latter (DWJ) causes a lower height. This clearly benefits the jet material removal process by facilitating water drainage from the crater and reducing the water cushion effect. Furthermore, the specific energy of DWJ is nearly one-tenth that of CWJ, indicating a significantly higher energy utilization efficiency. These results provide a figure of merit for the application of DWJ in the surface processing of ductile material.

3.3.2. *Characteristics of erosion crater*

The size characteristics of the erosion crater formed by DWJ were obtained respectively, including entrance area, depth and erosion volume, as shown in Fig. 10. Under limited exposure time and waterjet pressure ($t = 60$s, and $p = 15$ MPa), no significant material removal can be detected by the optical profilometer on target surface. It is because that the material removal under limited impact velocity requires more exposure time to accumulate enough target damage, consistent with the relevant conclusions in previous results [34]. With increasing exposure time, the damage accumulates until the formation of detectable material failure. During 60–120s at 15 MPa, notable variations were observed in both the entrance area and depth, but the resulting material removal accounted for merely 0.36% of the overall column stacking diagram. As the exposure time further extended from 120 to 300s, the increase in entrance area exhibited minimal changes, whereas the depth nearly doubled, leading to a 10.2% increase in erosion volume. This indicates that the augmented material removal during this process is predominantly influenced by the increased depth.

At 20 MPa, the most significant increase in both the entrance area and erosion volume occurs at 120–300s, while the maximum depth increase takes place within the 0–60s. In previous studies about the material removal by waterjet

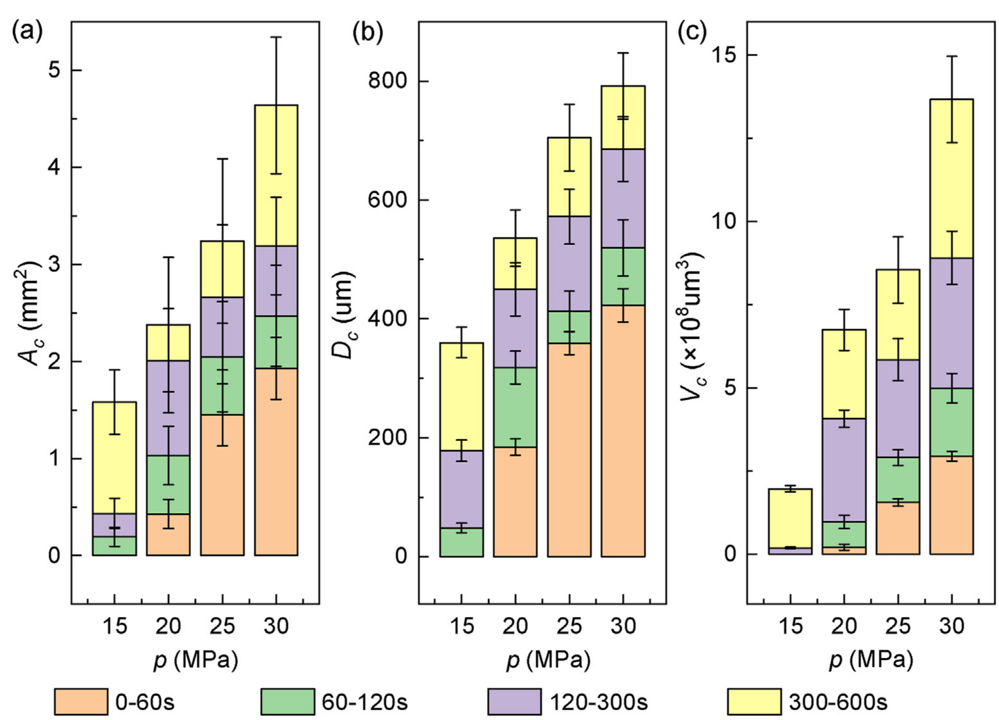

Fig. 10 – Entrance area (A_c), depth (D_c) and erosion volume (V_c) of erosion crater.

impact, it was commonly considered that material removal primarily occurs at the initial stage of waterjet impact [34,40]. However, these results demonstrate that the evolution of material removal over time is influenced not only by material and waterjet parameters but also by the chosen evaluation index (entrance area, depth or erosion volume). When the waterjet pressure experiences substantial increases (25 and 30 MPa), the largest growth in entrance area and depth indeed occurs during the earlier stage, but the growth of erosion volume exhibits more complex changes at different stages.

3.3.3. *Erosion intensity and energy consumption*

Under repeated liquid impingement, a typical curve of material removal is usually divided into four zones, respectively the incubation, accumulation, attenuation, and steady zone. It is shown as the growth rate of the characteristic parameters of the erosion crater in Fig. 11. These zones represent the most significant mechanism of material removal in the respective stages and have been able to predict or regulate the material removal process. For example, the primary aspect (surface erosion, bottom erosion, or internal wall erosion) of material removal can be determined by analyzing the growth rate changes of erosion crater characteristics at each stage. Then, the main mechanism of material removal can be inferred in each stage combined with the load characteristics of DWJ.

The growth rate (crater depth, entrance area, and volume) and specific energy of material removal for all the specimens are shown in Fig. 12. Overall, the growth rates of depth and volume under different pressures are consistent with the trend of the metal material erosion curve (Fig. 11). When the pressure is at 15 and 30 MPa, the growth rate of entrance area increases slightly during the 300–600s timeframe (Fig. 12(b)), which may be attributed to the deflection of the waterjet head and the recently emphasized subsurface perforation phenomenon [34,41]. Under limited waterjet energy ($p = 15$ MPa, $t = 60$s), no significant material removal and crater formation can be observed by the optical profilometer, and it corresponds to the incubation zone. During this period, plastic deformation occurs on the material surface, together with the change of micro properties and damage accumulation [42]. As the waterjet pressure increases, there is a clear acceleration in the material removal process. Notably, at higher pressures (20, 25, 30 MPa), the incubation zone periods are less than 60 s.

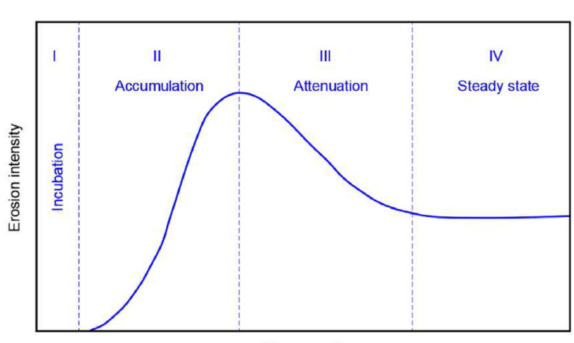

Fig. 11 – Typical erosion curve of metals by repeated liquid impacts.

After an initial mass loss, further waterjet energy results in severe material removal. The presence of critical parameters for material removal gives rise to varying trends in the growth rate of crater parameters (depth, coverage area, and erosion volume) under 20 MPa. Specifically, during the 0–60 s period, the growth rate of depth reaches its peak (Fig. 12(a)), while the growth rates of coverage area and crater volume continue to increase thereafter (Fig. 12(b) and (c)). This suggests that the increase in crater volume during this stage is largely due to the expansion of the entrance area. In 120–300s, although the growth rate of depth and area is not significant, that of crater volume reaches its peak, indicating that the removal of wall material is the dominant factor.

With further waterjet energy, the liquid gathering in the eroded crater can cushion the loadings transmitted to the material surface. More energy is consumed for the cavitation induced by the liquid shearing in the erosion crater. The growth rate of material removal decreases due to the energy attenuation (attenuation zone). As shown in Fig. 12(a), the material removal process at 20 MPa experiences accumulation and attenuation zones, and both the processes at 25 MPa and 30 MPa are consistent with attenuation zones. These results show that the waterjet pressure and exposure time together determine the material removal process.

It is worth noting that the specific energy and the growth rate of crater volume have an opposite trend under different waterjet pressure (Fig. 12(d)). Under 15 MPa, the specific energy of material removal in the incubation period reaches maximum. This is because the shear forces exerted by the low-pressure waterjet cannot directly remove the surface material, but only rely on the low fatigue stress to promote the crack growth, which ultimately segments the target material [34]. These results reveal that the high growth rate of material removal corresponds to low specific energy.

3.4. *Fractography*

Fig. 13 shows the crater fractography formed by the DWJ (S11, S12) and CWJ (S19). Obviously, the protuberant lips and folding deformation appear at the crater entrance. These surface unevenness results from the extrusion of surrounding materials, providing an area for loading shear forces [43]. Due to the dynamic loads, the material can be removed at the waterjet pressure below the material strength [34]. It can be observed that many material fragments still have a weak connection with the target (S11-1, S11-2 and S11-3). As the exposure time increases to 600s, the most of fragments in the impact area are removed, leaving some cracks and pits (S12-1, S12-1, and S12-3). Since the coverage area of the crater entrance has exceeded the impact range, the hydraulic penetration induced by lateral jetting has likely become the primary cause of material removal.

The microtopography resulting from CWJ is illustrated in S19. Some protuberant lips curl outward and cover a part of the target surface beyond the crater entrance. Under the quasi-static lateral loads, these deformed lips still connect to the target. But for DWJ, the folding deformation at the crater edge extends outwards to a certain range. Although the obvious deformation occurs on the crater edges, the

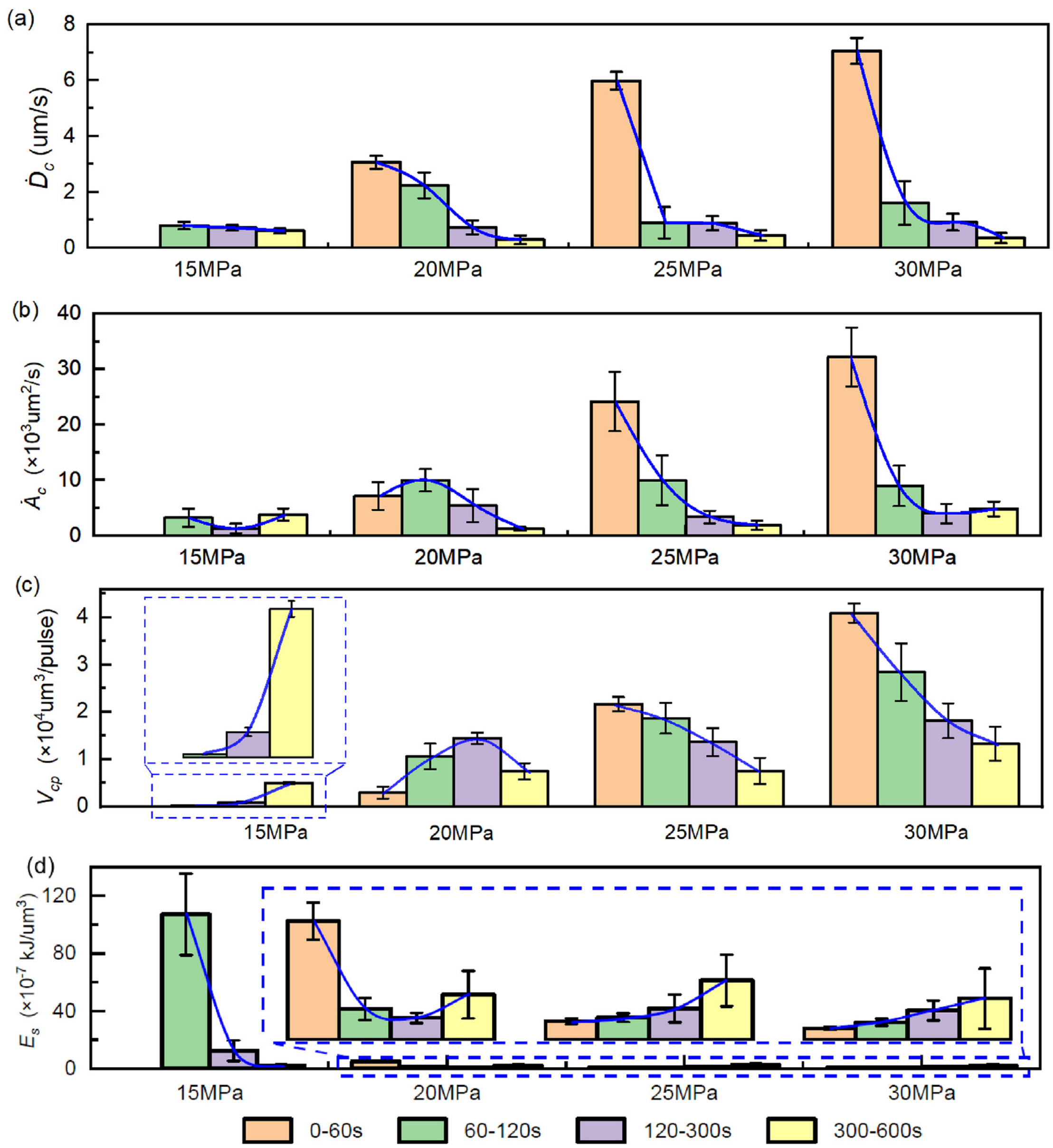

Fig. 12 – Changes in growth rate and specific energy. (a) Growth rate of crater depth; (b) growth rate of area; (c) growth rate of crater volume per slug; (d) specific energy.

protuberant crater lips are mostly sheared off, indicating that the periodic lateral jetting has better performance in removing the protuberant materials.

4. Discussion

Following the mechanical disruption, the loading patterns of conventional CWJ have undergone significant modifications, as depicted in Fig. 14. The loading patterns of DWJ exhibits four distinct features: repeated, discrete, transient, and asymmetric. The former three are attributed to discontinuities in the flow field structure, while the latter is a consequence of jet structure deflection.

Firstly, the repeated impact of the waterjet produces an alternating load in the form of water hammer pressure, stagnation pressure, or high shear forces. This alternating load can cause fatigue damage [42,43], as confirmed by the smooth fracture surface shown in Fig. 13. Secondly, the discrete structure of the waterjet creates intervals between adjacent water masses, preventing the accumulation of water in the erosion crater and reducing the water cushion effect. The discrete structure also enables accurate control over various water slug parameters (such as quantity, frequency, diameter, and length), thereby improving the control over jet energy. Furthermore, the continuous and transient impacts of the waterjet lead to hammer pressures, stress waves, and high-speed radial flows, which work together to enhance the waterjet's material removal efficiency. Finally, the deflection of the waterjet's flow field changes the energy distribution, resulting in a larger coverage area of the crater and an increase in the velocity of the waterjet's head.

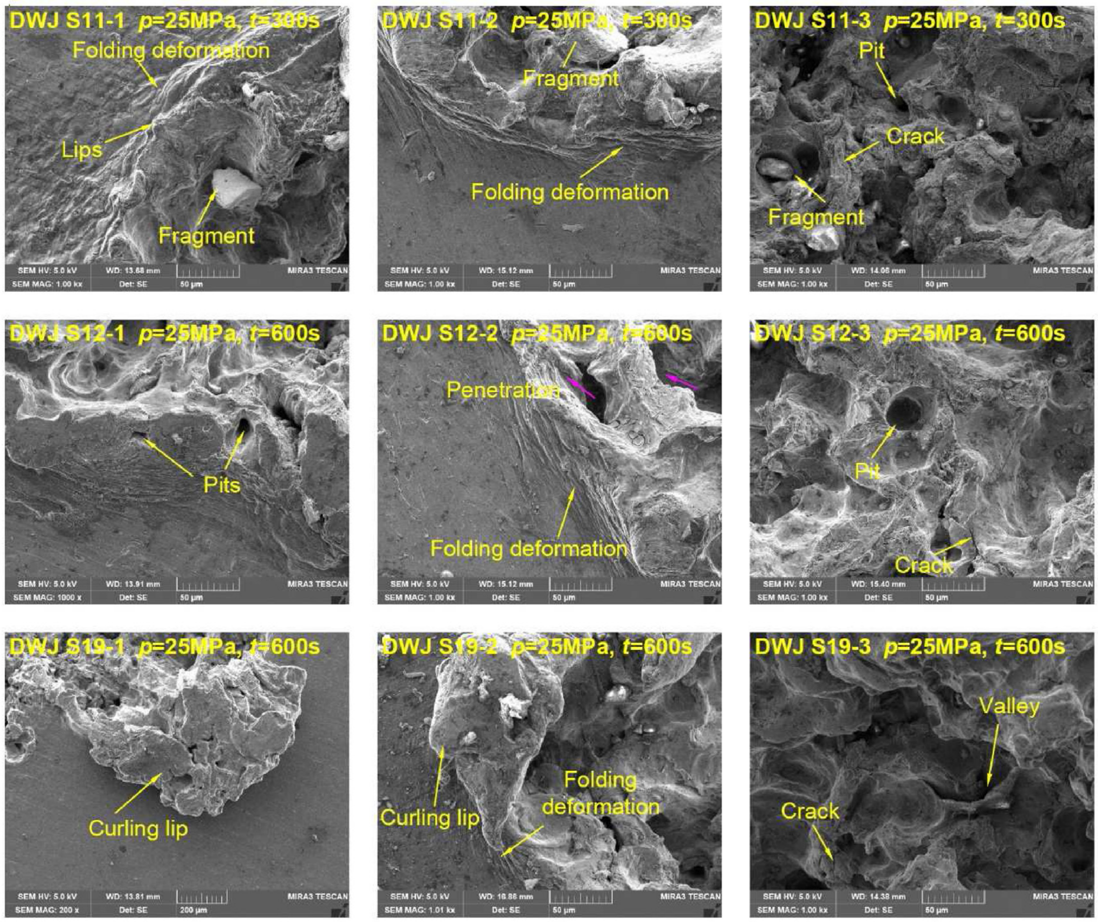

Fig. 13 – Fractography caused by DWJ and CWJ.

Fig. 15 demonstrates the material removal process through schematic diagrams and corresponding Scanning Electron Microscope (SEM) images. In the early stage of the process, the direct impact of the waterjet perpendicular to the material surface does not remove the material effectively. However, it can cause plastic deformation on the surface of the target material, resulting in rougher surfaces with protuberant lips and concave craters (as shown in Fig. 15(a)).

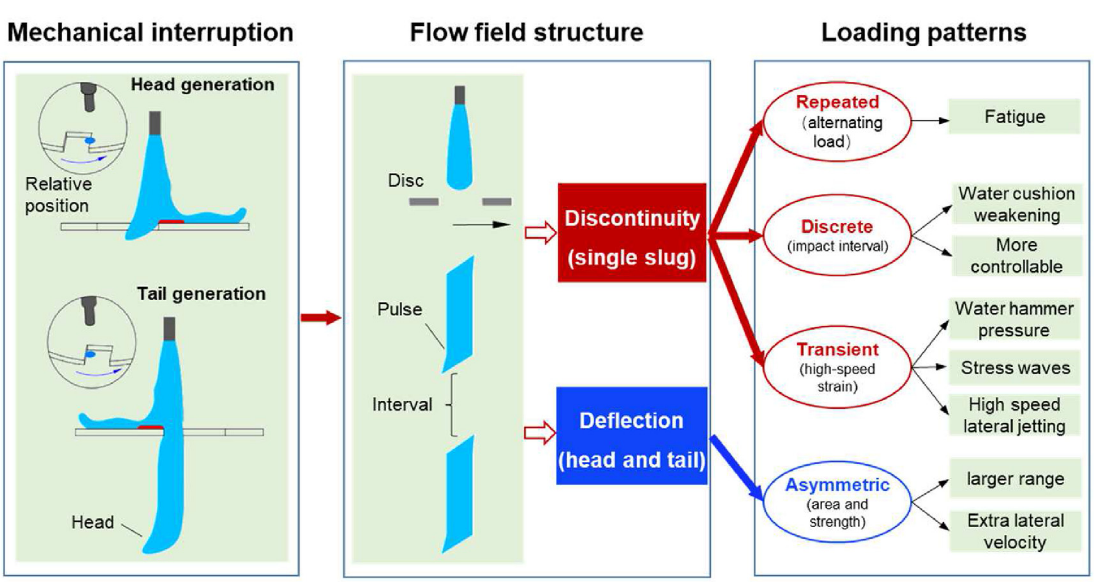

Fig. 14 – Schematic diagram of loading patterns of DWJ.

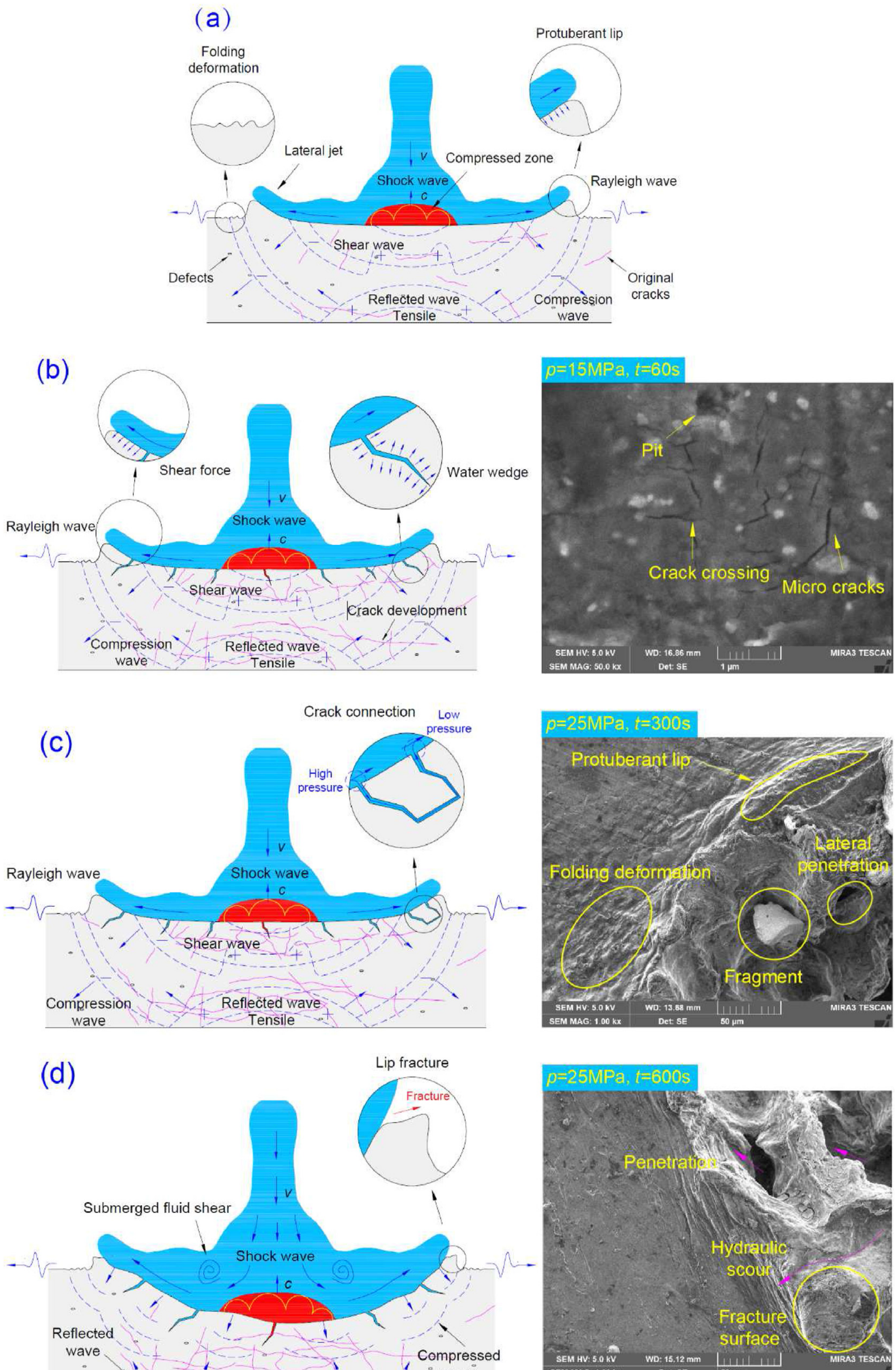

Fig. 15 – Schematic diagram of the material removal process and SEM figures. (a) formation of folding deformation and protuberant lips; (b) damage accumulation and surface fractures; (c) formation of the independent fragment for crack connection; (d) crater formation due to extensive material removal.

Once these deformations occur, the stress concentration increases due to the changes in surface shape, ultimately leading to pitting and cracking due to the hammer pressure and lateral jetting. For example, in section 3.2, no significant material removal can be observed by the optical profiler with 60s at 15 MPa. Nevertheless, micro pits and cracks were detected in the impact area, as presented in Fig. 15(b).

The cracks on the target surface are intermingled with subsurface defects caused by the dynamic water wedge pressure, ultimately leading to the complete separation of a fragment, as depicted in Fig. 15(c). Once the fragments are extricated from the target, radial penetration pits are left behind, thereby creating an opportunity for the formation of a subsurface micro tunnel.

Finally, the extensive material removal sets in, deepening the crater with successive impact of the waterjet through the normal impact pressure, lateral jetting, and water wedge pressure (as portrayed in Fig. 15(d)). During the latter stages of material removal, the liquid accumulates in the crater, thereby reducing the direct impact on the material surface.

Throughout the process, the protuberant lips are continually sheared away, and the smooth fracture surface indicates that it is not only the consequence of static shear forces but also fatigue loading under cyclic impact.

This study highlights the benefits of using DWJ for material removal, showcasing its potential for diverse industrial applications such as coating and rust removal, and cutting. Moreover, removing the protuberant lip also demonstrates the ability to polish rough surfaces. The next step involves conducting a comprehensive analysis of the technological parameters and the corresponding DWJ generation system, which could bring about several opportunities for green and high-quality industrial development.

5. Conclusions

The main conclusions of this study are as follows.

(1) The numerical results show that the transient velocity of the waterjet head increased by 53.0% because of the mechanical interruption at 30 MPa, and the pressure distribution on the target surface exhibited typical unsymmetric features.
(2) DWJ leads to an asymmetric crater and a U-shaped cross-sectional profile, reflecting the spatial inhomogeneity of material removal. In the later erosion stages, this characteristic causes a tapering groove to form along the crater edge.
(3) The crater area, depth, and volume formed by DWJ are 18.0%, 12.6% and 37.5% more than that of CWJ, respectively, and the height of the crater lip and specific energy are only the 82.0% and 9.2% of CWJ, respectively. At higher pressures, the growth rates of crater area, depth, and volume occur in the initial stage, while the specific energy decreases with the waterjet pressure.
(4) The material removal of ductile target is divided into the following stages: surface deformation due to the cyclic normal impact pressure, surface fracture owning to the local stress concentration near the deformation unevenness, formation of independent fragment mainly resulting from the water wedge pressure, and extensive material removal caused by the cyclic above processes.

Declaration of competing interest

The authors declare that they have no known competing financial interests or personal relationships that could have appeared to influence the work reported in this paper.

Acknowledgements

The authors appreciate the financial support from the National Nature Science Foundation of China (NSFC, No. 12002052, No. 12272053 and No. 12072038).

REFERENCES

[1] Zhang X, Wiśniewski P, Dykas S, Zhang G. Permeability enhancement properties of high-pressure abrasive water jet flushing and its application in a soft coal seam. Front Energy Res 2021;9. https://doi.org/10.3389/fenrg.2021.679623.
[2] Yu R, Dong X, Li Z, Fan M. A coupled SPH–DEM model for erosion process of solid surface by abrasive water-jet impact. Comput Times Part Mech 2023. https://doi.org/10.1007/s40571-023-00555-4.
[3] Wang C, Loh YM, Cheung CF, Liang X, Zhang Z, Ho LT. Post processing of additively manufactured 316L stainless steel by multi-jet polishing method. J Mater Res Technol 2023;23. https://doi.org/10.1016/j.jmrt.2023.01.054.
[4] Wang X, Zhao J, Liu S, Geng T. A constraint multi-step prediction method for identification of a water-jet vessel in 3DOF planar motion. Ocean Eng 2021;237. https://doi.org/10.1016/j.oceaneng.2021.109534.
[5] Azarsa E, Cinco L, Papini M. Fabrication of high aspect ratio free-standing structures using abrasive water jet micromachining. J Mater Process Technol 2020;275. https://doi.org/10.1016/j.jmatprotec.2019.116318.
[6] Wang Z, Liao Z, Axinte D, Dong X, Xu D, Augustinavicius G. Analytical model for predicting residual stresses in abrasive waterjet peening. Mater Des 2021:212. https://doi.org/10.1016/j.matdes.2021.110209.
[7] Haghbin N, Spelt JK, Papini M. Abrasive waterjet micromachining of channels in metals: comparison between machining in air and submerged in water. Int J Mach Tool Manufact 2015;88. https://doi.org/10.1016/j.ijmachtools.2014.09.012.
[8] Liu X, Liang Z, Wen G, Yuan X. Waterjet machining and research developments : a review. Int J Adv Manuf Technol 2019;102:1257–335. https://doi.org/10.1007/s00170-018-3094-3.
[9] Khan MA, Soni H, Mashinini PM, Uthayakumar M. Abrasive water jet cutting process form machining metals and composites for engineering applications: a review. Eng Res Express 2021;3. https://doi.org/10.1088/2631-8695/abfe98.
[10] Liu GY, Wang KK, Chen XX, Dong LM, Zhu DM, Zhang SJ. Numerical simulation of internal flow field for post-mixed abrasive water jet descaling nozzle. Chinese J Eng 2015;37. https://doi.org/10.13374/j.issn2095-9389.2015.s1.006.

[11] Xie J, Rittel D. A two-dimensional model for metallic surface roughness resulting from pure waterjet peening. Int J Eng Sci 2017;120:189–98. https://doi.org/10.1016/j.ijengsci.2017.08.010.
[12] Liao Z, Sanchez I, Xu D, Axinte D, Augustinavicius G, Wretland A. Dual-processing by abrasive waterjet machining—a method for machining and surface modification of nickel-based superalloy. J Mater Process Technol 2020;285. https://doi.org/10.1016/j.jmatprotec.2020.116768.
[13] Cook SS. Erosion by water-hammer. Proc R Soc A 1928;119:481–8. https://doi.org/10.1098/rspa.1928.0107.
[14] Brunton JH. A discussion on deformation of solids by the impact of liquids, and its relation to rain damage in aircraft and missiles, to blade erosion in steam turbines, and to cavitation erosion - high speed liquid impact. Phil Trans Roy Soc Lond Math Phys Sci 1966;260:79–85. https://doi.org/10.1098/rsta.1966.0031.
[15] Kennedy CF, Field JE. Damage threshold velocities for liquid impact. J Mater Sci 2000;35:5331–9. https://doi.org/10.1023/A:1004842828161.
[16] Nag A, Hloch S, Dixit AR, Pude F. Utilization of ultrasonically forced pulsating water jet decaying for bone cement removal. Int J Adv Manuf Technol 2020;110:829–40. https://doi.org/10.1007/s00170-020-05892-9/.
[17] Ling Y, Ge Z, Tang J, Lu Y, Zhang Y, Wang L. Development of a hydraulically controlled piston-pressurized pulsed water jet device and its application potential for hard rock breaking. Rev Sci Instrum 2021;92. https://doi.org/10.1063/5.0052853.
[18] Zhang Y, Lu Y, Tang J, Ling Y, Wang L, Yao Q, et al. Development and application of rock breaking platform with variable cross section extrusion pulsed water jet. J Mech Sci Technol 2022;36. https://doi.org/10.1007/s12206-022-0516-9.
[19] Huang F, Li S, Zhao Y, Liu Y. A numerical study on the transient impulsive pressure of a water jet impacting nonplanar solid surfaces. J Mech Sci Technol 2018;32:4209–21. https://doi.org/10.1007/s12206-018-0819-z.
[20] Xue Y, Si H, Hu Q. The propagation of stress waves in rock impacted by a pulsed water jet. Powder Technol 2017;320:179–90. https://doi.org/10.1016/j.powtec.2017.06.047.
[21] Raj P, Hloch S, Tripathi R, Srivastava M, Nag A, Klichová D, et al. Investigation of sandstone erosion by continuous and pulsed water jets. J Manuf Process 2019;42:121–30. https://doi.org/10.1016/j.jmapro.2019.04.035.
[22] Yuan M, Li D, Kang Y, Shi H, Pan H. Characteristics of oscillation in cavity of helmholtz nozzle generating self-excited pulsed waterjet. Chin J Mech Eng 2022;35. https://doi.org/10.1186/s10033-022-00714-3.
[23] Foldyna J, Sitek L, Švehla B, Švehla Š. Utilization of ultrasound to enhance high-speed water jet effects. Ultrason Sonochem 2004;11:131. https://doi.org/10.1016/j.ultsonch.2004.01.008. Elsevier.
[24] Hloch S, Srivastava M, Nag A, Müller M, Hromasová M, Svobodová J, et al. Effect of pressure of pulsating water jet moving along stair trajectory on erosion depth, surface morphology and microhardness. Wear 2020:452–3. https://doi.org/10.1016/j.wear.2020.203278.
[25] Srivastava M, Nag A, Chattopadhyaya S, Hloch S. Standoff distance in ultrasonic pulsating water jet. Materials 2021;14:1–18. https://doi.org/10.3390/ma14010088.
[26] Tobin EF, Young TM, Raps D, Rohr O. Comparison of liquid impingement results from whirling arm and water-jet rain erosion test facilities. Wear 2011;271. https://doi.org/10.1016/j.wear.2011.02.023.
[27] Jackson MJ. Non-traditional machining using pulsed water jets. Int J Manuf Technol Manag 2005;7. https://doi.org/10.1504/IJMTM.2005.006827.
[28] Vijay MM, Remisz J, Shen X. Potential of pulsed water jets for cutting and fracturing of hard rock formations. Int J Surf Min Reclamat Environ 1993;7:121–32. https://doi.org/10.1080/17480939308547572.
[29] Jackson MJ, Ahmed W. Micro and nanomanufacturingvol. 2; 2017. https://doi.org/10.1007/978-3-319-67132-1.
[30] Dehkhoda S, Hood M. The internal failure of rock samples subjected to pulsed water jet impacts. Int J Rock Mech Min Sci 2014;66:91–6. https://doi.org/10.1016/j.ijrmms.2013.12.021.
[31] Dehkhoda S, Hood M. An experimental study of surface and sub-surface damage in pulsed water-jet breakage of rocks. Int J Rock Mech Min Sci 2013;63:138–47. https://doi.org/10.1016/j.ijrmms.2013.08.013.
[32] Polyakov AA, Zhabin A, Averin E, Polyakov AA. Generalized equation for calculating rock cutting efficiency by pulsed water jets. J Rock Mech Geotech Eng 2019;11:867–73. https://doi.org/10.1016/j.jrmge.2018.11.009.
[33] Wang Z, Kang Y, Wang X, Li D, Shi H. Effects of modulation position on the impact performance of mechanically modulated pulsed water jet. J Manuf Process 2020;56:510–21. https://doi.org/10.1016/j.jmapro.2020.05.011.
[34] Wang Z, Kang Y, Xie F, Shi H, Wu N, Wang Z, et al. Experimental investigation on the penetration characteristics of low-frequency impact of pulsed water jet. Wear 2022:488–9. https://doi.org/10.1016/j.wear.2021.204145.
[35] Yamagata T, Hasegawa M, Fujisawa N. Erosion behavior of pulsed-jet test facility for wind turbine blade. Wear 2023:514–5. https://doi.org/10.1016/j.wear.2022.204565.
[36] Paul S, Hoogstrate AM, Van Luttervelt CA, Kals HJJ. Analytical and experimental modelling of the abrasive water jet cutting of ductile materials. J Mater Process Technol 1998;73. https://doi.org/10.1016/S0924-0136(97)00228-8.
[37] Žunić J, Hirota K. Measuring shape circularity. Lect Notes Comput Sci 2008;5197. https://doi.org/10.1007/978-3-540-85920-8_12. LNCS.
[38] Lu Z, Cheng Y, Hood M, Lu Y, Tadic D. Comparative experimental and mechanism study of hard-rock erosion by pulsed water jet with the same power. 2019.
[39] Miao X, Wu M, Cui C, Jie D, He R, Wang H, et al. Microstructure and water erosion resistance of in situ synthesized (TiBx+TiC)/Ti composite coatings produced by laser cladding. J Mater Res Technol 2023:23. https://doi.org/10.1016/j.jmrt.2023.02.067.
[40] Liu Y, Wei J, Ren T, Lu Z. Experimental study of flow field structure of interrupted pulsed water jet and breakage of hard rock. Int J Rock Mech Min Sci 2015;78:253–61. https://doi.org/10.1016/j.ijrmms.2015.06.005.
[41] Hloch S, Souček K, Svobodová J, Hromasová M, Müller M. Subsurface microtunneling in ductile material caused by multiple droplet impingement at subsonic speeds. Wear 2022:490–1. https://doi.org/10.1016/j.wear.2021.204176.
[42] Gunasckaran M, Rudy SL, Thiruvengadam A. Experimental and analytical investigations on multiple liquid impact erosion. 1970.
[43] Azhari A, Schindler C, Nkoumbou J, Kerscher E. Surface erosion of carbon steel 1045 during waterjet peening. J Mater Eng Perform 2014;23:1870–80. https://doi.org/10.1007/s11665-014-0932-9. Springer New York LLC.